

SCIENTIFIC REPORTS



OPEN

Earth's youngest banded iron formation implies ferruginous conditions in the Early Cambrian ocean

Zhi-Quan Li^{1,2,3}, Lian-Chang Zhang², Chun-Ji Xue¹, Meng-Tian Zheng², Ming-Tian Zhu², Leslie J. Robbins³, John F. Slack⁴, Noah J. Planavsky⁵ & Kurt O. Konhauser³

It has been proposed that anoxic and iron-rich (ferruginous) marine conditions were common through most of Earth history. This view represents a major shift in our understanding of the evolution of marine chemistry. However, thus far, evidence for ferruginous conditions comes predominantly from Fe-speciation data. Given debate over these records, new evidence for Fe-rich marine conditions is a requisite if we are to shift our view regarding evolution of the marine redox landscape. Here we present strong evidence for ferruginous conditions by describing a suite of Fe-rich chemical sedimentary rocks—banded iron formation (BIF)—deposited during the Early Cambrian in western China. Specifically, we provide new U-Pb geochronological data that confirm a depositional age of ca. 527 Ma for this unit, as well as rare earth element (REE) data are consistent with anoxic deposition. Similar to many Algoma-type Precambrian iron formations, these Early Cambrian sediments precipitated in a back-arc rift basin setting, where hydrothermally sourced iron drove the deposition of a BIF-like protolith, the youngest ever reported of regional extent without direct links to volcanogenic massive sulphide (VMS) deposits. Their presence indicates that marine environments were still characterized by chemical- and redox-stratification, thus supporting the view that—despite a dearth of modern marine analogues—ferruginous conditions continued to locally be a feature of early Phanerozoic seawater.

It is well established that the Archaean and Palaeoproterozoic Earth was characterized by anoxic, ferruginous oceans, as evidenced by the deposition, and subsequent cessation of, large-scale BIFs^{1,2}. Traditionally, the oceans were envisioned to have become predominantly oxic³ or euxinic^{4,5} around 1.8 Ga, coincident with deposition of the last economic iron formation. These traditional views were challenged, and it was later suggested that ferruginous conditions were a common feature after the end of BIF deposition⁶. In a series of seminal papers, Canfield and colleagues proposed that ferruginous conditions were common in the mid-Ediacaran (580–560 Ma)⁷. It was subsequently proposed that ferruginous conditions were prevalent during Earth's middle history^{8,9}, and even into the Cambrian¹⁰ during the early diversification of animals and establishment of trophically complex ecosystems¹¹.

Current evidence for ferruginous conditions in the Cambrian comes mainly from Fe-speciation data for marine shales, a calibrated proxy that relies on linking ratios of biogeochemically active iron phases, such as sulphides, carbonates, and oxides, to water-column redox conditions^{8,12}. However, Fe-speciation signatures can be ambiguous. Critically, a range of modern marine settings, foremost sediments deposited in relatively near-shore settings, display Fe-speciation patterns equivalent to those linked to ferruginous conditions^{13–17}. Moreover, detailed petrographic work has suggested that common diagenetic processes can lead to ambiguous Fe-speciation signatures and specifically false signals of ferruginous conditions¹⁸. Numerous studies have drawn on alternative methods for tracking ocean anoxia in the Cambrian, including the use of redox-sensitive trace element

¹State Key Laboratory of Geological Processes and Mineral Resources, China University of Geosciences, Beijing, 100083, China. ²Key Laboratory of Mineral Resources, Institute of Geology and Geophysics, Chinese Academy of Sciences, Beijing, 100029, China. ³Department of Earth and Atmospheric Sciences, University of Alberta, Edmonton, Alberta, T6G 2E3, Canada. ⁴U.S. Geological Survey, National Center, MS 954, Reston, Virginia, 20192, USA. ⁵Department of Geology and Geophysics, Yale University, New Haven, Connecticut, 06520, USA. Correspondence and requests for materials should be addressed to L.-C.Z. (email: lczhang@mail.iggcas.ac.cn) or C.-J.X. (email: chunji.xue@cugb.edu.cn)

enrichments or carbon and sulphur stable isotopes^{19–21}. Additionally, non-traditional stable isotopes, such as those for uranium²² or molybdenum^{23,24}, have been used to directly track euxinia in the Cambrian, but critically, not ferruginous conditions. Although anoxia is a prerequisite to euxinia, strong euxinic conditions develop as the result of abundant organic carbon export and strong bacterial sulphate reduction driving elevated sulphide concentrations. However, these conditions are unlikely to be representative of background marine environments⁸.

Similar to what is observed in the Archaean and periodically through the rest of the Precambrian^{1,2}, the presence of iron-rich chemical sedimentary rocks (i.e., BIFs), can provide a clear signature of ferruginous conditions. However, until now, there have been no extensive, basin-scale marine Fe-rich chemical sedimentary rocks reported from the Lower Cambrian that would be indicative of widespread ferruginous conditions during this critical transition in Earth history. In this paper, we couple geochronological data with mineralogy, sedimentary features, and REE systematics from a suite of Fe-rich chemical sedimentary rocks in the Taxkorgan terrane, western China, and provide strong evidence for ferruginous conditions in the Early Cambrian. Importantly, these sedimentary rocks closely resemble Archaean Algoma-type BIF, sedimentary rocks that formed close to volcanic arcs and spreading centres, having been produced by exhalative hydrothermal processes related to submarine volcanism in either partially closed basins or open seawater systems²⁵. As such, our newly described BIFs are the only regionally extensive examples of this type thus far reported from the Phanerozoic, without having spatial and stratigraphic links to known VMS deposits.

Results

Sedimentary features and mineralogy. The Taxkorgan terrane occurs within the West Kunlun orogenic belt, southwest of the Tarim block. The region is dominated by the Bulunkuole (Pt₁) and Bulunkuole (C₁) Groups (Fig. 1a,b)^{26,27}. Strata of the Bulunkuole Group are monoclinical, striking 358°–45°, with moderate to steep dips ranging from 20° to 75°. The strata consist of metasedimentary rocks (e.g., biotite-quartz schist), metavolcanic rocks (e.g., metabasalt, metadacite), Fe-rich sedimentary rocks, and dolomitic marble that experienced green-schist- to amphibolites-facies metamorphism during the Caledonian orogeny (492–428 Ma)²⁸. Corresponding protoliths were most likely greywacke, volcanoclastic rocks, bimodal volcanics (dacite and basalt), iron formation, and carbonates. A description of the regional geology is provided in the Supplementary Information. The Fe-rich chemical sediments mainly occur in the Jierteike, Yelike, Taaxi, Zankan, and Laobing areas (Fig. 1c). All of these strata trend NW to SE and formed as part of an extensive belt that contains more than 500 Mt of known iron ore, with a prospective aggregate size reaching 1 Gt. We limited our sampling to the Jierteike, Yelike, and Taaxi areas because the strata there did not experience significant post-depositional alteration (i.e., fewer veins, fracture zones, and intrusions), and are compositionally analogous to typical Precambrian BIF. In terms of areal extent, these three Fe-rich deposits have surface dimensions of 31 km², 18 km², and 8 km² for the Yelike, Jierteike, and Taaxi areas, respectively. Collectively, these three main areas preserve over 90 Mt of iron ore.

The Fe-rich chemical sediments display laminated and lenticular structures and are typically interlayered with metasedimentary rocks (biotite-quartz schist) in outcrop, and locally are in contact with meta-volcanoclastic rocks and dolomitic marble in drill core. Rocks below the Fe-rich chemical sedimentary rocks are dominated by meta-volcanics (30 m thick) and dolomitic marble (>50 m). The main host rock, biotite-quartz schist, has a medium- to fine-grained lepidoblastic texture, as well as schistose and banded structures. This schist is well bedded, and alternates with the Fe-rich sedimentary rocks (Fig. 2a), displaying typical sedimentary features. Ratios of immobile trace elements in the biotite-quartz schist (Nb/Y; Ti/Zr, Fig. S1) are similar to those of metadacites in the region, suggesting that the schist has a major felsic volcanic component, consistent with Th/Sc ratios of 1.07–1.13 (Table S1). Although the BIF locally shows “S-type” and other folds, primary banding structures are preserved (Fig. 2b). Constituents are predominantly quartz (~60%) and lesser biotite (~20%), with minor chlorite (~12%) and magnetite (~3%). The biotite tends to be fine grained, 0.3–1.2 mm in size, and locally replaces chlorite.

The Fe-rich sedimentary rocks are characterized by Fe-rich layers, composed of magnetite, and Si-rich layers, composed mostly of quartz, with lesser calcite, biotite, and magnetite (Fig. 2c,d). Bulk compositions are dominated by iron (FeO 29.03–77.8 wt.%) and silica (SiO₂ 18.0–56.3 wt.%) (Table S2); BIFs are compositionally defined as having a Fe concentration within this range (i.e., at least 15 wt.% Fe)²⁹. Magnetite is anhedral, and locally together with quartz, displays a blastoplastic texture, including similar grain sizes and a clear paragenetic link. Martite is common within the oxidized ores and locally replaces magnetite crystals in the BIF (Fig. 2e). No pyrite was found within the BIF; the only pyrite observed is near fracture zones (Fig. 2f), characteristic of a secondary origin.

Geochronology of the Jierteike area. Previous studies on the age of the Bulunkuole Group have suggested either a Palaeoproterozoic³⁰ or early Paleozoic age^{31–33}, and until now the depositional age has remained unresolved. Palaeoproterozoic zircons can normally be found within the southern section of the Bulunkuole Group near the Zankan iron deposit, whereas early Paleozoic zircons occur in several different locations^{27,34}. Zhang *et al.*²⁶ suggested that these contrasting zircon ages may be reconciled by dividing the Bulunkuole Group into two parts: (1) Palaeoproterozoic strata in the south, which include the Zankan and Mokaer areas, and (2) Cambrian strata in the Yelike, Taaxi, and Laobing areas that extend from the southwest to the northeast. The Jierteike area, studied here, lies between Taaxi-Laobing and Zankan-Mokaer. Knowing the exact age of the Jierteike BIF is, therefore, critical for resolving the age and genesis of this deposit.

We analyzed U-Pb isotopes in zircon to constrain the age of the BIF, which previously was interpreted as either Cambrian or Palaeoproterozoic²⁶. BIFs in the Jierteike area are conformable, stratiform, and interbedded with biotite-quartz schist. Therefore, the schist can be used to constrain the formational age of the BIF. The location of the biotite-quartz schist sample 15TJE1-1, from which zircons were obtained, is shown in Fig. 3. Many of the zircons are euhedral to subhedral, 100–140 μm in length, with large length-to-width ratios (up to 3). Concentric zoning is common in these zircons, sharing typical features of zircons crystallized from granitic magma. The sharp edges

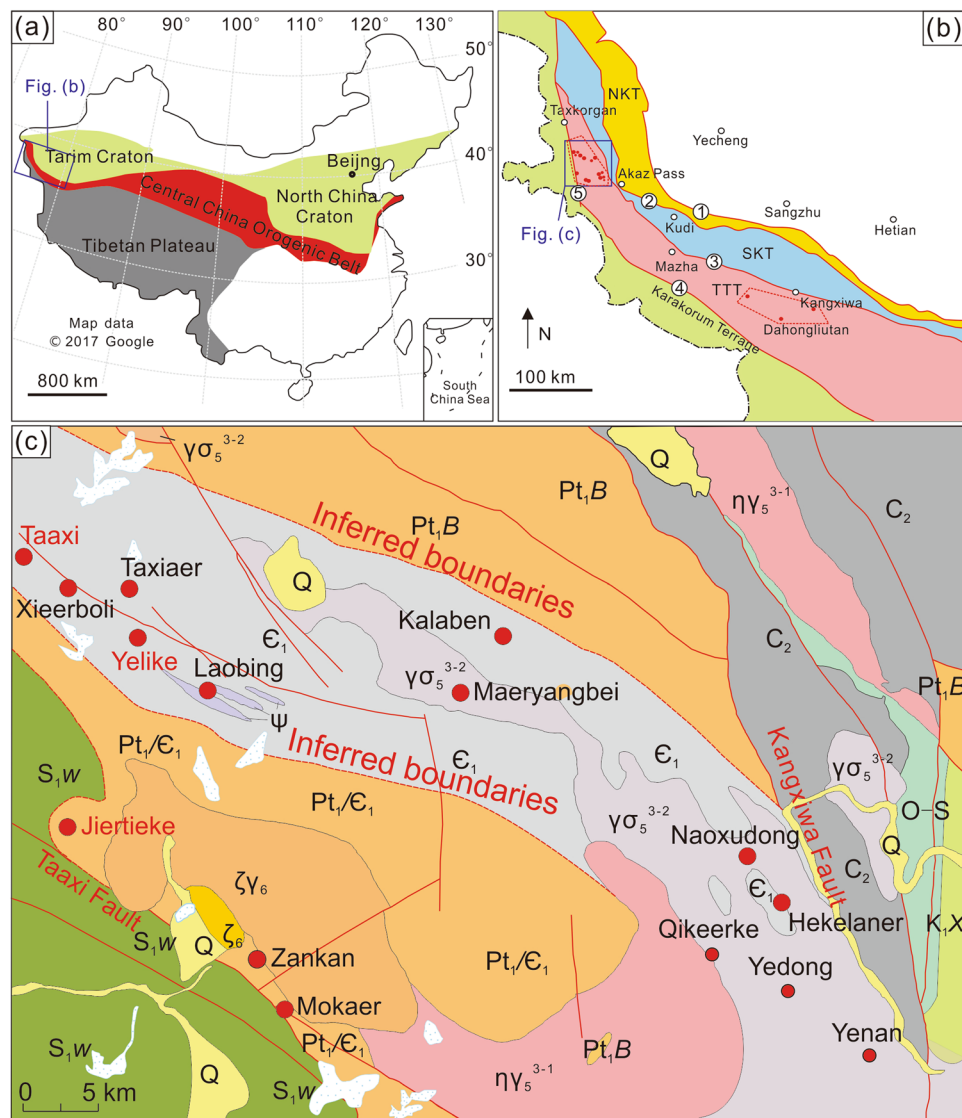


Figure 1. (a) Tectonic subdivisions of China and location of Western Kunlun orogenic belt; (b) Tectonic subdivisions of West Kunlun orogenic belt, showing Taxkorgan region, location of Fe deposits and basins are marked by red dots and dashed lines, respectively. (c) Geological map and distribution of metasedimentary Fe deposits in south Taxkorgan area; Legend: NKT: North Kunlun Terrane, SKT: South Kunlun Terrane, TTT: Taxkorgan-Tianshuihai Terrane, ①: Oytag-Kegang Fault, ②: Kudi Fault, ③: Kangxiwa Fault, ④: Longmucuo-Shuanghu Fault, ⑤: Karakorum Fault; Q: Quaternary, K₁X: Cretaceous, C₂: late Carboniferous, S₁W: early Silurian, O-S: Ordovician-Silurian, E₁: Early Cambrian, Pt₁/E₁: Early Proterozoic or Early Cambrian, Pt₁B: Early Proterozoic, ζ₆: Himalayan syenite, ζ₆γ: Himalayan syenogranite, γσ₅³⁻²: Yanshanian granodiorite, ηγ₅³⁻¹: Yanshanian monzonitic granite, ψ: Pyroxenite, red spots are locations of iron-rich sediments. Figure 1a was made with data from Google Maps (<https://www.google.com/maps>), and reproduced using CorelDRAW x7 (<http://www.coreldraw.com/en/>). Figure 1b,c were after refs^{26,27}.

likely reflect short-distance transport, potentially from the metadacite in the region (see above). Most of the zircons lack overgrowth rims (Fig. 3), suggesting that late-stage processes, such as metamorphism, had minimal if any post-crystallization effects. *In situ* spot analyses for U, Th, and Pb were conducted on 22 subhedral to euhedral zircon grains, which have variable Th and U contents with Th/U ratios ranging from 0.57–1.11, suggesting an origin as magmatic zircon. Most grains yielded ²⁰⁶Pb/²³⁸U ages between 547.5 to 513 Ma, with a Concordia Age of 527.5 ± 3.4 Ma (MSWD = 0.082) (see Supplementary Table S3), which is similar to the weighted average age ($n = 16$) of 527.5 ± 9.9 Ma (MSWD = 0.15). These ages correspond with those of the Taaxi metadacite (553–531 Ma; 524–520 Ma)^{27,34}, suggesting that the zircon grains are derived from the coeval dacite in the region (Fig. 3). Moreover, a recent detailed geochronological study of U-Pb ages of zircons from a granitic intrusion in the central section of the Bulunkuo Group (close to Jiertieke), yielded an age of 510–513 Ma³⁵, which can be used to constrain the lower limit of the formational age. Given this evidence for an Early Cambrian depositional age, the critical question becomes how did the BIFs precipitate, and crucially, what information can they provide about Early Cambrian redox conditions?

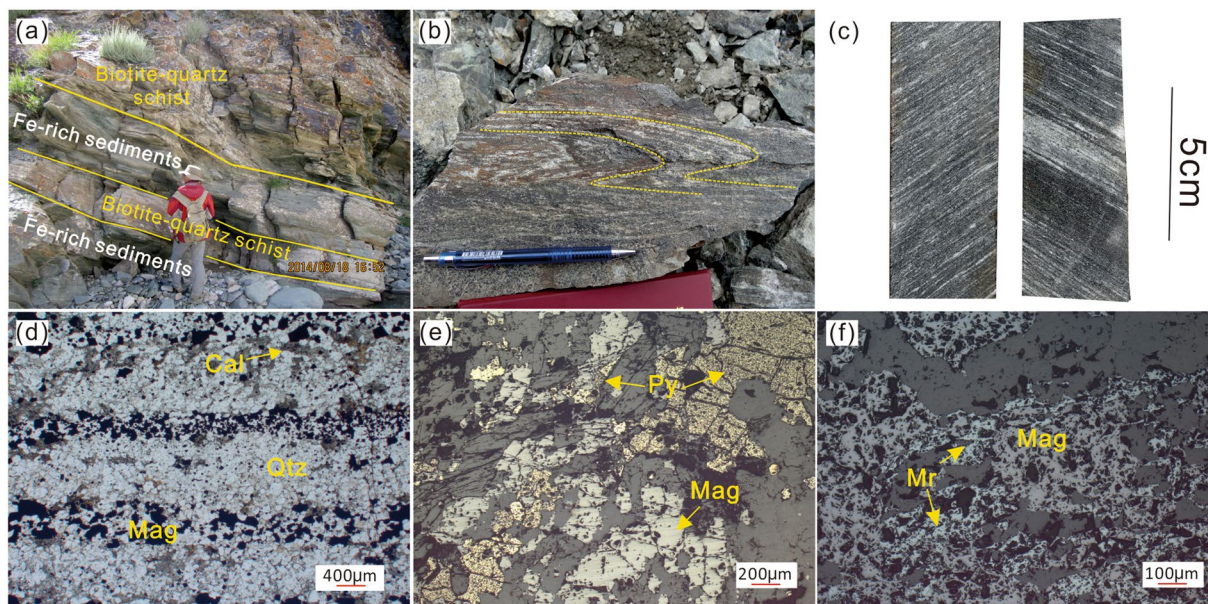


Figure 2. (a) Well-bedded biotite-quartz schist alternating with BIF; (b) “S-type” folds in BIF retain initial banded structure; (c,d) BIF shows characteristic Fe-rich (dark) and Si-rich (light) layers; (e) Pyrite replaces euhedral magnetite crystal near a fracture zone; (f) Martite replacement of magnetite grain. Abbreviation: Mag-magnetite, Qtz-quartz, Cal-calcite, Py-pyrite, Mr-martite.

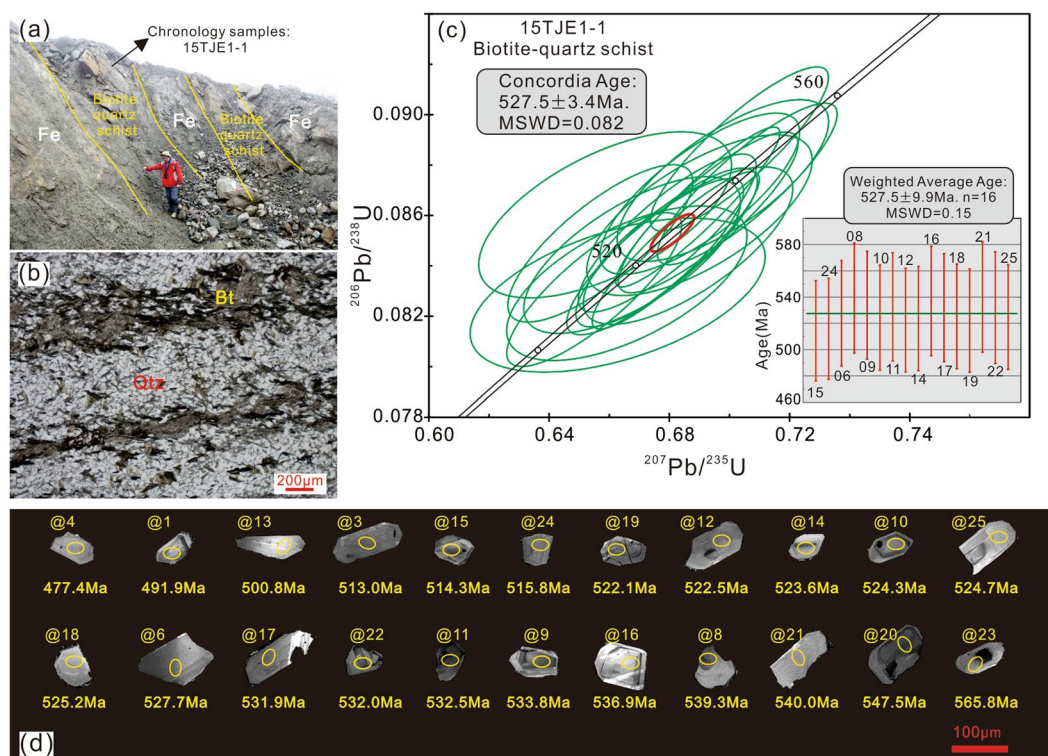


Figure 3. (a) Outcrop photo showing location of samples used for geochronological analyses; (b) thin section photo in plane polarized light of biotite-quartz schist; (c) Concordia plot and weighted average plot for zircon U-Pb ages from biotite-quartz schist; (d) SEM cathodoluminescence images with corresponding apparent ages of zircons from biotite-quartz schist; note lack of rounded grains.

Major and trace elements of the iron-rich chemical sediments. In addition to FeO and SiO₂, other oxides present above trace levels include CaO (0.41–15.2 wt.%), MgO (0.11–7.16 wt.%), MnO (0.01–1.05 wt.%), K₂O (0.00–0.65 wt.%), TiO₂ (0.01–0.28 wt.%), and P₂O₅ (0.03–0.16 wt.%). Locally high Mn concentrations

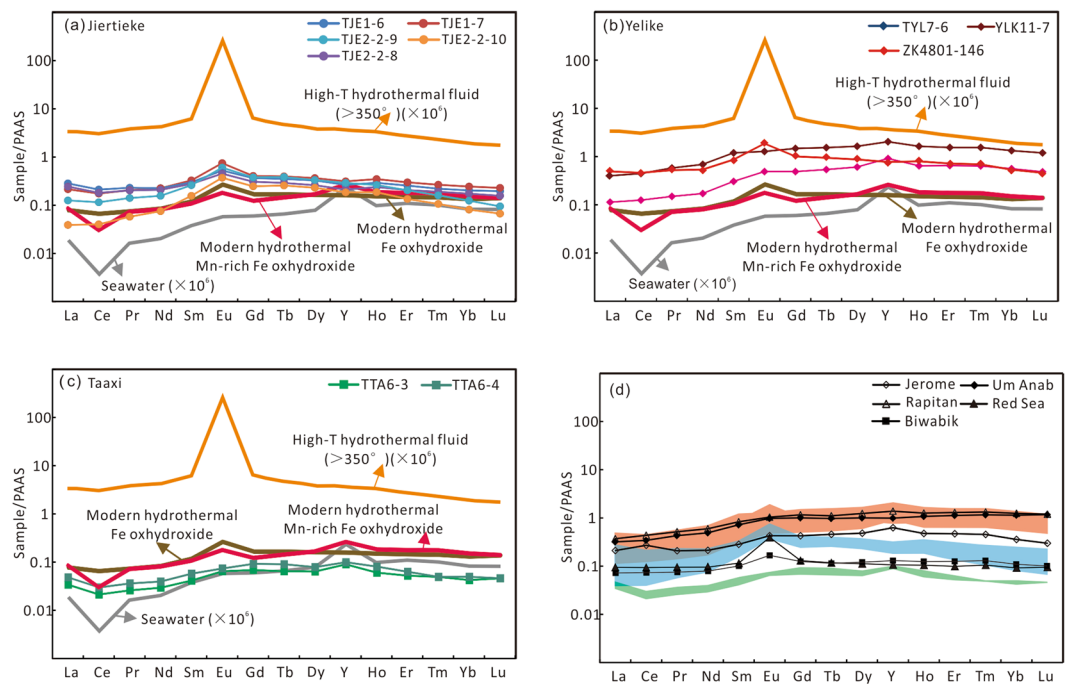


Figure 4. REE systematics of the BIF from (a) Jierteike, (b) Yelike, and (c) Taaxi regions. Average South Pacific seawater, average high-T (>350 °C) hydrothermal fluid⁷⁰, as well as modern oxalic hydrothermal Fe-oxyhydroxide and Mn-rich Fe-oxyhydroxide samples⁴⁹ are plotted for comparison. (d) Taxkorgan Fe-rich sediments relative to averages from several Palaeoproterozoic and Neoproterozoic BIF, including 1.74 Ga Jerome Formation (U.S.A.)⁴⁶, 1.88 Ga Biwabik BIF (Animikie basin, U.S.A.)⁷¹, 715 Ma Rapitan Iron Formation (Canada)⁷², and 750 Ma Um Anab Formation (Egypt)⁷³, as well as modern Fe-rich sediments from Atlantis II Deep (Red Sea)⁷⁴. Samples from Jierteike (blue), Yelike (red), and Taaxi (green) regions are highlighted. All data are normalized to PAAS values after McLennan⁷⁵.

suggest that a significant flux of Mn(II) was brought into the basin, a condition consistent with, but not entirely dependent upon, anoxia in the deep part of the water column³⁶. The BIFs from Jierteike and Taaxi also have lower Al_2O_3 and Na_2O contents ($\text{Al}_2\text{O}_3 = 0.09\text{--}1.48$ wt.%; $\text{Na}_2\text{O} = 0.02\text{--}0.74$ wt.%) compared to Yelike ($\text{Al}_2\text{O}_3 = 4.80\text{--}5.55$ wt.%; $\text{Na}_2\text{O} = 1.67\text{--}3.01$ wt.%). The important point here is that, although the major-element compositions indicate some detrital input to the BIF, the Fe-rich sedimentary rocks are predominantly chemical in origin.

Rare earth element data are one of the most commonly used geochemical tools to understand the origin of chemical sedimentary rocks such as BIF^{37–41}. In particular, REE patterns can indicate whether the Fe-rich sediments formed in, or near, the chemocline in a redox-stratified ferruginous basin. Further, the REE system is typically rock-buffered during the diagenesis and metamorphic alteration of chemical precipitates^{42–44}, and thus is a powerful tool to track water-column redox conditions coeval with deposition^{39,45,46}. Multiple aspects of the REE system are directly (Ce anomalies) or indirectly (light to heavy REE ratios, Y/Ho ratios) sensitive to redox conditions. Cerium can be oxidized from its trivalent to tetravalent state, which results in a large decrease in solubility; however, below the redoxcline, Ce can become reductively recycled, and negative Ce anomalies indicative of oxygenic conditions may disappear⁴⁷. Additionally, owing to differences in particle reactivity in seawater, light REE depletion and large positive Y anomalies develop in oxic seawater. Within anoxic seawater, dissolution of oxides results in the suppression of Y anomalies and a shift to flat or even light REE-enriched patterns⁴¹.

REE patterns in iron oxide-rich sedimentary rocks have been extensively used to track marine redox conditions^{1,2,41}. Although iron oxides do not perfectly capture dissolved REE patterns in experiments⁴⁵, hydrous iron oxides that precipitated in the water column can record patterns of dissolved REE in seawater e.g. ref.⁴⁸). Similarly, although iron oxides precipitated at low pH can develop strong positive Ce anomalies⁴⁵, these conditions are not relevant to marine environments distal from hydrothermal vents. As a modern example of the utility of REE patterns in iron oxides, their distribution at Loihi Seamount trace the shift from deposition within low-oxygen, iron-rich waters to fully oxic conditions⁴⁹ (Fig. 4). Accordingly, iron oxides forming in low-oxygen waters (e.g., at chemocline of redox-stratified basins) should have a small or positive Ce anomaly, and less-pronounced light REE depletion and Y anomalies, than would be expected for oxic seawater. Taking this into account, REE can be used to track the presence of ferruginous waters in a basin. Some fractionation of REE among various mineral phases may result from diagenesis and metamorphism, but critically, the REE patterns of Fe minerals (e.g., magnetite and hematite) tend to correspond well to bulk-rock patterns⁵⁰. Furthermore, bulk digestion methods, such as those employed here, yield seawater-like REE patterns, thus providing confidence that an authigenic signal is being preserved^{41,51–53}.

Iron-rich sedimentary rocks from the Yelike and Taaxi areas lack significant negative Ce anomalies (Fig. 5), but display features consistent with an authigenic, rather than detrital, origin of the REE. These features include

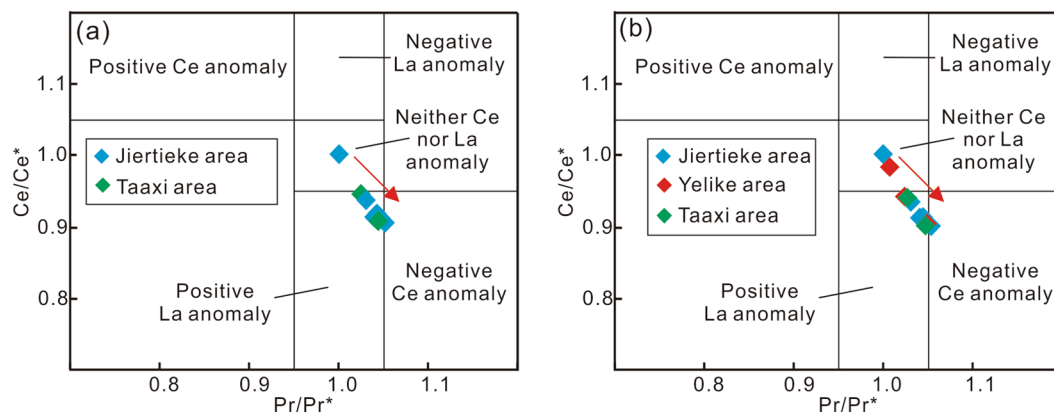


Figure 5. (a) Ce/Ce^* - Pr/Pr^* cross-plot indicates there are no true negative Ce anomalies for Taxkorgan Fe-rich sediments. Samples from Yelike region are excluded due to suspected detrital contamination; (b) Recalculated detrital-free basis using PAAS as detrital component and Hf as normalizing element (Table S4), lacks true negative Ce anomalies like the uncorrected bulk samples. Ce/Ce^* was calculated as $Ce/Ce^* = Ce_{PAAS} / (2Pr_{PAAS} - Nd_{PAAS})$, Pr/Pr^* was calculated as $Pr/Pr^* = 2Pr_{PAAS} / (Ce_{PAAS} + Nd_{PAAS})$, after Bolhar *et al.*⁵⁷.

positive Y anomalies (1.25–1.46), slight light REE depletion ($La/Yb_{PAAS} = 0.20–0.97$), and bulge among the middle REE (Fig. 4). As such, the REE patterns presented here are unlikely to reflect detrital signatures. Moreover, the above-mentioned features are indicative of authigenic REE sorption to iron oxides at, or near, a chemocline. Given the absence of negative Ce anomalies, the adsorption of REE likely took place within anoxic, rather than fully oxic, waters^{41,45,54}. The REE patterns, together with the presence of magnetite-quartz layers and lack of associated VMS deposits (see below), suggests that the depositional style of the Early Cambrian Bulunkuole Group is broadly analogous to that of Precambrian BIFs, rather than of distal hydrothermal deposits that formed within anoxic ocean basin^{41,55,56}. Samples from the Yelike and Jiertieke regions similarly record authigenic REE signatures (e.g., light REE depletion and variable Y/Ho ratios), and a lack of negative Ce anomalies.

Bolhar *et al.*⁵⁷ suggested that terrestrial material (i.e., felsic and basaltic crust) is characterized by a near-constant Y/Ho ratio of ~ 26 . As a consequence, admixtures of any detrital terrestrial contaminant should be evident through co-variation of Y/Ho ratios and detrital contaminants such as Al_2O_3 and Zr. However, only a weak correlation is apparent between Zr-Y/Ho and Al_2O_3 -Y/Ho, as well as correlations with $\sum REE + Y$ and Y/Y* (Fig. S2), thus effectively ruling out a detrital control on the Y/Ho ratios and REE patterns. Consistent with this view, near-chondritic Y/Ho ratios are found in samples having the lowest detrital input (e.g., TJE2-2-9, TJE2-2-10; indicated by low Al_2O_3 , TiO_2 , and Zr contents; Table S2). Moreover, REE data calculated on a detrital-free basis (using PAAS as the detrital component and Hf as the normalizing element) display the same REE patterns, Ce and Eu anomalies (Table S4, $Ce/Ce^* = 0.90–1.00$; $Eu/Eu^* = 0.98–2.15$) as the uncorrected bulk samples (Fig. S3). This supports that REE signatures are not controlled by detrital overprinting. Thus, the presented REE data point to primary iron oxyhydroxide particles deposited from a predominantly anoxic water column, with a loss of Y occurring below the chemocline, thereby explaining the concurrent absence of a negative Ce anomaly and depressed Y/Ho ratios (Fig. 4).

Discussion and Conclusions

Previous research has argued that the West Kunlun orogenic belt, relevant to the Tarim block^{58,59} and its neighboring regions, formed by a back-arc extensional tectonic event linked to the proto-Tethys Ocean subduction and seafloor spreading^{58,60}. The Tarim block broke away from the northern side of the Australia block, and then drifted from the supercontinent Gondwana⁶¹. This model has recently been supported by Gao *et al.*³⁴ based on study of the Taxkorgan region in West Kunlun. Ages for a metabasalt (516 Ma) and metadacite (521 Ma) in the Taaxi region likely represent depositional ages of bimodal volcanic rocks in the Early Cambrian, associated with the extensional event³⁴ that led to the formation of a back-arc rift basin²⁷. After the breakup of Gondwana, the Tarim block drifted northwest into the proto-Tethys Ocean, leading to a broad rift within the open ocean (Zhang *et al.*³⁵, see their figure 14, and Li & Powell⁶¹, see their figure 7). In addition to the Taxkorgan Fe-rich basins studied herein, the Dahongliutan hematitic BIF⁶² has recently been discovered to the east of the Western Kunlun orogenic belt, south of the Tarim block (formational age: 593–532 Ma), while on the opposite side of the rift in northern Australia, Fe-rich chemical sediments were similarly deposited⁶³. The temporal and spatial correspondence of these deposits indicates that the Fe-rich sediments were spatially widespread. Furthermore, although a large number of volcanogenic massive sulfide (VMS) deposits are present in western China (e.g., Qilian and Altai-Junggar), the closest known VMS deposit of early Paleozoic age is more than 2000 km from our study area, and significantly these VMS deposits are mainly younger than Late Cambrian⁶⁴, thus suggesting that the Taxkorgan Fe-rich sedimentary rocks are unrelated to VMS systems in western China. Hence, similar to Archaean Algoma-type BIF that formed in back-arc basins¹, the Lower Cambrian BIF examined here formed in a basin that was likely influenced by an enhanced hydrothermal iron flux, but critically, that marine conditions within that basin (i.e., persistent widespread ferruginous and anoxic waters) were fundamentally different than those in modern oceans.

Consistent with this view, the distribution of REE patterns in the Jierteike BIF suggests that the basin was relatively broad and unlikely to have contained extremely stratified waters (e.g., like the modern Red Sea). Foremost, we have found significant positive Eu anomalies exist, the magnitude of these anomalies varies considerably within strata of the iron belts, suggesting multiple REE sources and significant REE scavenging. Specifically, the lack of Eu anomalies in the Yelike and Taaxi regions is inconsistent with the formation of the Fe deposits within a small, strongly stratified basin, where one would expect persistent strong positive Eu anomalies. We therefore suggest that records from this basin can provide a glimpse into redox evolution with a Cambrian marine basin, rather than simply representing an anomalous setting.

Based on the new geochronology data presented here, coupled with sedimentological, mineralogical, and geochemical data on the BIF, we provide evidence for the deposition of a series of large-scale, Early Cambrian Fe-rich chemical sediments. Based on differences in REE patterns, these Fe-rich sediments can be distinguished from modern Fe-exhalite deposits (e.g., lack of Eu anomalies in Taaxi and Yelike), and indicate a genesis similar to that proposed for Archean Algoma-type BIF²⁵. The absence of true negative Ce anomalies in the chemical sedimentary rocks suggests that marine anoxia and ferruginous conditions extended well into the Early Cambrian, offering support for recent Fe-speciation studies^{7,11}, and indicating that the Early Cambrian was characterized, at least locally, by stratified, redox-heterogeneous basins^{65,66}.

Methods

Major elements. Major element oxide abundances for bulk iron-rich sedimentary rock samples were determined using an X-ray fluorescence spectrometer with an analytical error of less than 5% at ALS Chemex (Guangzhou, China). Loss on ignition (LOI) was determined by heating powders at 1000 °C for 2 hours. Decreased weights of the powders were then calculated.

Trace elements. Samples were broken into chips, with any chips showing evidence of veins or secondary alteration removed, and the remaining sample was then ground to a fine powder in a tungsten steel grinding mill. About 50 mg of the powder was weighed, then dissolved in 1 mL concentrated HF and 1 mL 8 M HNO₃ in a 15 mL Savillex™ Teflon vial. The temperature was maintained at 130 °C for 48 hours. Following this step, 2 mL of 8 M HNO₃ was added immediately before the solution was evaporated to dryness at 130 °C. Following evaporation, 2 mL of 8 M HNO₃ was added to achieve complete dissolution of the sample. After the solution cooled, samples were transferred to polyethylene bottles containing 50 g 2% HNO₃ and a 10 ng g⁻¹ internal indium standard. Trace element concentrations were analyzed on an Element I Finnigan MAT inductively coupled plasma-mass spectrometer (ICP-MS) at the Institute of Geology and Geophysics, Chinese Academy of Sciences (IGGCAS), Beijing. Two standard samples, FER-1 and FER-2, were used to monitor analyses. The accuracy of measured concentrations is 1 to 5%.

U-Pb zircon geochronology. The outcrop sample used for geochronology was taken from interlayered biotite-quartz schist occurring within Fe-rich sedimentary rocks. Conventional magnetic and density techniques were used to separate zircons from the sample. Zircons were then mounted in epoxy resin and polished to section the crystals for imaging and analysis. Transmitted and reflected light micrographs, as well as cathodoluminescence (CL) images, were taken using a CAMECA electron microprobe (EMPA) at IGGCAS. The CL images were used to reveal the internal structures and zoning of the zircons. Thorium and Pb isotopes were then analyzed on a Cameca 1280 secondary ion mass spectrometer (SIMS) at the IGGCAS. The operating procedure and subsequent calculations have been described previously in detail⁶⁷. A common Pb correction was carried out based on the interference- and background-corrected ²⁰⁴Pb signal and a model Pb composition⁶⁸. Uncertainties on individual analysis in the data are reported at the 1σ level; mean ages for U/Pb (and Pb/Pb) analyses are presented with a 95% confidence interval, and the data were plotted using ISOPLOT⁶⁹.

References

1. Bekker, A. *et al.* Iron formations: their origins and implications for ancient seawater chemistry. *Treatise on Geochemistry* **12**, 561–628 (2014).
2. Konhauser, K. O. *et al.* Iron formations: a global record of Neoproterozoic to Palaeoproterozoic environmental history. *Earth-Science Reviews* **172**, 140–177 (2017).
3. Holland, H. D. The oxygenation of the atmosphere and oceans. *Philosophical Transactions of the Royal Society of London B: Biological Sciences* **361**, 903–915 (2006).
4. Canfield, D. E. A new model for Proterozoic ocean chemistry. *Nature* **396**, 450–453 (1998).
5. Shen, Y., Canfield, D. E. & Knoll, A. H. Middle Proterozoic ocean chemistry: evidence from the McArthur Basin, northern Australia. *American Journal of Science* **302**, 81–109 (2002).
6. Poulton, S. W., Fralick, P. W. & Canfield, D. E. Spatial variability in oceanic redox structure 1.8 billion years ago. *Nature Geoscience* **3**, 486–490 (2010).
7. Canfield, D. E. *et al.* Ferruginous conditions dominated later Neoproterozoic deep-water chemistry. *Science* **321**, 949–952 (2008).
8. Poulton, S. W. & Canfield, D. E. Ferruginous conditions: a dominant feature of the ocean through Earth's history. *Elements* **7**, 107–112 (2011).
9. Planavsky, N. J. *et al.* Widespread iron-rich conditions in the Mid-Proterozoic ocean. *Nature* **477**, 448–451 (2011).
10. Goldberg, T., Strauss, H., Guo, Q. & Liu, C. Reconstructing marine redox conditions for the Early Cambrian Yangtze Platform: evidence from biogenic sulphur and organic carbon isotopes. *Palaeogeography, Palaeoclimatology, Palaeoecology* **254**, 175–193 (2007).
11. Sperling, E. A. *et al.* Statistical analysis of iron geochemical data suggests limited Late Proterozoic oxygenation. *Nature* **523**, 451–454 (2015).
12. Poulton, S. W. & Canfield, D. E. Development of a sequential extraction procedure for iron: implications for iron partitioning in continentally derived particulates. *Chemical Geology* **214**, 209–221 (2005).

13. Scholz, F., Severmann, S., McManus, J. & Hensen, C. Beyond the Black Sea paradigm: the sedimentary fingerprint of an open-marine iron shuttle. *Geochimica et Cosmochimica Acta* **127**, 368–380 (2014).
14. Riedinger, N. *et al.* Sulfur cycling in an iron oxide-dominated, dynamic marine depositional system: the Argentine continental margin. *Frontiers in Earth Science* **5**, <https://doi.org/10.3389/feart.2017.00033> (2017).
15. Goldberg, T. *et al.* Controls on Mo isotope fractionations in a Mn-rich anoxic marine sediment, Gullmar Fjord, Sweden. *Chemical Geology* **296**, 73–82 (2012).
16. Aquilina, A., Homoky, W. B., Hawkes, J. A., Lyons, T. W. & Mills, R. A. Hydrothermal sediments are a source of water column Fe and Mn in the Bransfield Strait, Antarctica. *Geochimica et Cosmochimica Acta* **137**, 64–80 (2014).
17. Henkel, S., Kasten, S., Poulton, S. W. & Staubwasser, M. Determination of the stable iron isotopic composition of sequentially leached iron phases in marine sediments. *Chemical Geology* **421**, 93–102 (2016).
18. Slotznick, S. P., Eiler, J. M. & Fischer, W. W. The effects of metamorphism on iron mineralogy and the iron speciation redox proxy. *Geochimica et Cosmochimica Acta* (in press).
19. Zhuravlev, A. Y. & Wood, R. A. Anoxia as the cause of the Mid-Early Cambrian (Botomian) extinction event. *Geology* **24**, 311–314 (1996).
20. Gill, B. C. *et al.* Geochemical evidence for widespread euxinia in the later Cambrian ocean. *Nature* **469**, 80–83 (2011).
21. Och, L. M. *et al.* Redox changes in Early Cambrian black shales at Xiaotan section, Yunnan Province, South China. *Precambrian Research* **225**, 166–189 (2013).
22. Dahl, T. W. *et al.* Uranium isotopes distinguish two geochemically distinct stages during the later Cambrian SPICE event. *Earth and Planetary Science Letters* **401**, 313–326 (2014).
23. Jiang, S. Y. *et al.* Early Cambrian ocean anoxia in South China. *Nature* **459**, E5–E6 (2009).
24. Chen, X. *et al.* Rise to modern levels of ocean oxygenation coincided with the Cambrian radiation of animals. *Nature Communications* **6**, <https://doi.org/10.1038/ncomms8142> (2015).
25. Gourcerol, B., Thurston, P. C., Kontak, D. J., Côté-Mantha, O. & Biczok, J. Depositional setting of Algoma-type banded iron formation. *Precambrian Research* **281**, 47–79 (2016).
26. Zhang, L. C. *et al.* Metallogenic regularity of the Taxkorgan iron ore belt, West Kunlun. *Journal of Earth Sciences and Environment* **38**, 427–443 (2016).
27. Zheng, M. T. Ore-forming study of the Early Cambrian iron (barite) metallogenic sub-belt in the Taxkorgan iron polymetallic belt, West Kunlun. (Doctoral Dissertation. Beijing, University of Chinese Academy of Sciences) (2017).
28. Liu, W. P. *et al.* Geochemical characteristics and metamorphic P-T paths of the Bulunkuole Group in Taxkorgan, western Kunlun. *Acta Petrologica Sinica* **29**, 923–937 (2013).
29. James, H. L. Sedimentary facies of iron-formation. *Economic Geology* **49**, 235–293 (1954).
30. Ji, W. *et al.* The discovery of Palaeoproterozoic volcanic rocks in the Bulunkuoler Group from the Tianshuihai massif in Xinjiang of northwest China and its geological significance. *Science China Earth Sciences* **54**, 61–72 (2010).
31. Zhang, C., Lu, S., Yu, H. & Ye, H. Tectonic evolution of the western Kunlun orogenic belt in northern Qinghai-Tibet Plateau, evidence from zircon SHRIMP and LA-ICP-MS U-Pb geochronology. *Science in China Series D, Earth Sciences* **50**, 825–835 (2007).
32. Yan, C. H. *et al.* The discovery of the “Panir-type” iron ore deposits in Taxkorgan area of Xinjiang and its geological significance. *Geological Bulletin of China* **31**, 549–557 (2012).
33. Huang, C. Y. Geological characteristics and genesis of the iron ore deposit in Bulunkuole Group, West Kunlun, Xinjiang. (Doctoral Dissertation. Guangzhou, Guangzhou Institute of Geochemistry, Chinese Academy of Sciences) (2014).
34. Gao, X. F. *et al.* Origin of the volcanic rocks from the Ta’axi region, Taxkorgan Xinjiang and its geological significance. *Earth Science, Journal of China University of Geosciences* **38**, 1169–1182 (2013).
35. Zhang, C. L., Zou, H. B., Ye, X. T. & Chen, X. Y. Tectonic evolution of the NE section of the Pamir Plateau: new evidence from field observations and zircon U-Pb geochronology. *Tectonophysics* **723**, 27–40 (2018).
36. Roy, S. Sedimentary manganese metallogenesis in response to the evolution of the Earth system. *Earth-Science Reviews* **77**, 273–305 (2006).
37. Klein, C. & Beukes, N. J. Geochemistry and sedimentology of a facies transition from limestone to iron-formation deposition in the Early Proterozoic Transvaal Supergroup, South Africa. *Economic Geology* **84**, 1733–1774 (1989).
38. Derry, L. A. & Jacobsen, S. B. The chemical evolution of Precambrian seawater: evidence from REEs in banded iron formations. *Geochimica et Cosmochimica Acta* **54**, 2965–2977 (1990).
39. Bau, M. & Dulski, P. Distribution of yttrium and rare-earth elements in the Penge and Kuruman iron-formations, Transvaal Supergroup, South Africa. *Precambrian Research* **79**, 37–55 (1996).
40. Frei, R. *et al.* Trace element and isotopic characterization of Neoproterozoic and Paleoproterozoic iron formations in the Black Hills (South Dakota, USA): assessment of chemical change during 2.9–1.9 Ga deposition bracketing the 2.4–2.2 Ga first rise of atmospheric oxygen. *Precambrian Research* **162**, 441–474 (2008).
41. Planavsky, N. J. *et al.* Rare earth element and yttrium compositions of Archean and Paleoproterozoic Fe formations revisited: new perspectives on the significance and mechanisms of deposition. *Geochimica et Cosmochimica Acta* **74**, 6387–6405 (2010).
42. Bau, M. Rare-earth element mobility during hydrothermal and metamorphic fluid-rock interaction and the significance of the oxidation state of europium. *Chemical Geology* **93**, 219–230 (1991).
43. Bau, M. Effects of syn- and post-depositional processes on the rare-earth element distribution in Precambrian iron-formations. *European Journal of Mineralogy* **5**, 257–267 (1993).
44. Banner, J. L., Hanson, G. N. & Meyers, W. J. Rare earth element and Nd isotopic variations in regionally extensive dolomites from the Burlington-Keokuk Formation (Mississippian): implications for REE mobility during carbonate diagenesis. *Journal of Sedimentary Research* **58**, 415–432 (1988).
45. Bau, M. Scavenging of dissolved yttrium and rare earths by precipitating iron oxyhydroxide: experimental evidence for Ce oxidation, Y-Ho fractionation, and lanthanide tetrad effect. *Geochimica et Cosmochimica Acta* **63**, 67–77 (1999).
46. Slack, J. F. *et al.* Suboxic deep seawater in the late Paleoproterozoic: evidence from hematitic chert and iron formation related to seafloor-hydrothermal sulfide deposits, central Arizona, USA. *Earth and Planetary Science Letters* **255**, 243–256 (2007).
47. De Carlo, E. H. & Green, W. J. Rare earth elements in the water column of Lake Vanda, McMurdo Dry Valleys, Antarctica. *Geochimica et Cosmochimica Acta* **66**, 1323–1333 (2002).
48. Sherrill, R. M., Field, M. P. & Ravizza, G. Uptake and fractionation of rare earth elements on hydrothermal plume particles at 9°45' N, East Pacific Rise. *Geochimica et Cosmochimica Acta* **63**, 1709–1722 (1999).
49. Rouxel, O., Toner, B., Germain, Y. & Glazer, B. Geochemical and iron isotopic insights into hydrothermal iron oxyhydroxide deposit formation at Loihi Seamount. *Geochimica et Cosmochimica Acta* **220**, 449–482 (2018).
50. Alibert, C. Rare earth elements in Hamersley BIF minerals. *Geochimica et Cosmochimica Acta* **184**, 311–328 (2016).
51. Alexander, B. W., Bau, M., Andersson, P. & Dulski, P. Continentally-derived solutes in shallow Archean seawater: rare earth element and Nd isotope evidence in iron formation from the 2.9 Ga Pongola Supergroup, South Africa. *Geochimica et Cosmochimica Acta* **72**, 378–394 (2008).
52. Pecoits, E. *et al.* Petrography and geochemistry of the Dales Gorge banded iron formation: paragenetic sequence, source and implications for palaeo-ocean chemistry. *Precambrian Research* **172**, 163–187 (2009).

53. Haugaard, R., Pecoits, E., Lalonde, S., Rouxel, O. & Konhauser, K. The Joffre banded iron formation, Hamersley Group, Western Australia: assessing the palaeoenvironment through detailed petrology and chemostratigraphy. *Precambrian Research* **273**, 12–37 (2016).
54. Planavsky, N. J. *et al.* Iron-oxidizing microbial ecosystems thrived in late Paleoproterozoic redox-stratified oceans. *Earth and Planetary Science Letters* **286**, 230–242 (2009).
55. Hein, J. R., Gibbs, A. E., Clague, D. A. & Torresan, M. Hydrothermal mineralization along submarine rift zones, Hawaii. *Marine Georesources & Geotechnology* **14**, 177–203 (1996).
56. Prakash, L. S. *et al.* Distribution of REEs and yttrium among major geochemical phases of marine Fe–Mn-oxides: comparative study between hydrogenous and hydrothermal deposits. *Chemical Geology* **312**, 127–137 (2012).
57. Bolhar, R., Kamber, B. S., Moorbath, S., Fedo, C. M. & Whitehouse, M. J. Characterisation of Early Archaean chemical sediments by trace element signatures. *Earth and Planetary Science Letters* **222**, 43–60 (2004).
58. Mattern, F. & Schneider, W. Suturing of the proto- and paleo-Tethys oceans in the western Kunlun (Xinjiang, China). *Journal of Asian Earth Sciences* **18**, 637–650 (2000).
59. Zhu, J. *et al.* Geochemistry and petrogenesis of the early Palaeozoic appinite-granite complex in the Western Kunlun orogenic belt, NW China: implications for Palaeozoic tectonic evolution. *Geological Magazine*, <https://doi.org/10.1017/S0016756817000450> (2017).
60. Hu, J., Wang, H. & Wang, M. Provenance and tectonic setting of siliciclastic rocks associated with the Neoproterozoic Dahongliutan BIF: implications for the Precambrian crustal evolution of the Western Kunlun orogenic belt, NW China. *Journal of Asian Earth Sciences* **147**, 95–115 (2017).
61. Li, Z. X. & Powell, C. M. An outline of the palaeogeographic evolution of the Australasian region since the beginning of the Neoproterozoic. *Earth-Science Reviews* **53**, 237–277 (2001).
62. Hu, J., Wang, H. & Wang, M. Geochemistry and origin of the Neoproterozoic Dahongliutan banded iron formation (BIF) in the Western Kunlun orogenic belt, Xinjiang (NW China). *Ore Geology Reviews* **89**, 836–857 (2017).
63. Duhig, N. C., Davidson, G. J. & Stolz, J. Microbial involvement in the formation of Cambrian sea-floor silica-iron oxide deposits, Australia. *Geology* **20**, 511–514 (1992).
64. Wang, C., Deng, J., Zhang, S. & Yang, L. Metallogenic province and large scale mineralization of volcanogenic massive sulfide deposits in China. *Resource Geology* **60**, 404–413 (2010).
65. Li, C. *et al.* A stratified redox model for the Ediacaran ocean. *Science* **328**, 80–83 (2010).
66. Jin, C. *et al.* A highly redox-heterogeneous ocean in South China during the Early Cambrian (529–514 Ma): implications for biota-environment co-evolution. *Earth and Planetary Science Letters* **441**, 38–51 (2016).
67. Li, X. H., Liu, Y., Li, Q. L., Guo, C. H. & Chamberlain, K. R. Precise determination of Phanerozoic zircon Pb/Pb age by multicollector SIMS without external standardization. *Geochemistry, Geophysics, Geosystems* **10**, <https://doi.org/10.1029/2009GC002400> (2009).
68. Stacey, J. T. & Kramers, I. Approximation of terrestrial lead isotope evolution by a two-stage model. *Earth and Planetary Science Letters* **26**, 207–221 (1975).
69. Ludwig, K. R. Isoplot/Ex rev. 2.49: a geochronological tool kit for Microsoft Excel. *Berkeley Geochronology Center* **55** (2001).
70. Bolhar, R. & Van Kranendonk, M. J. A non-marine depositional setting for the northern Fortescue Group, Pilbara Craton, inferred from trace element geochemistry of stromatolitic carbonates. *Precambrian Research* **155**, 229–250 (2007).
71. Planavsky, N. J. Iron cycling and redox evolution in the Precambrian. (Doctoral Dissertation. Riverside, University of California) (2012).
72. Halverson, G. P. *et al.* Fe isotope and trace element geochemistry of the Neoproterozoic syn-glacial Rapitan Iron Formation. *Earth and Planetary Science Letters* **309**, 100–112 (2011).
73. Basta, F. F., Maurice, A. E., Fontboté, L. & Favarger, P. Y. Petrology and geochemistry of the banded iron formation (BIF) of Wadi Karim and Um Anab, Eastern Desert, Egypt, implications for the origin of Neoproterozoic BIF. *Precambrian Research* **187**, 277–292 (2011).
74. Laurila, T. E., Hannington, M. D., Petersen, S. & Garbe-Schönberg, D. Early depositional history of metalliferous sediments in the Atlantis II Deep of the Red Sea: evidence from rare earth element geochemistry. *Geochimica et Cosmochimica Acta* **126**, 146–168 (2014).
75. McLennan, S. M. Rare earth elements in sedimentary rocks; influence of provenance and sedimentary processes. *Reviews in Mineralogy and Geochemistry* **21**, 169–200 (1989).

Acknowledgements

This research was financially supported by the National Natural Science Foundation of China (Grant NO. 41372100 and U1703242) and National 305 Project (Grant NO. 2015BAB05B02). We appreciate Yanhai Hao, Haijun Wang, Yujun Shi, and other geological engineers from the NO. 2 Geological Party, and Xinjiang Bureau of Geology and Mineral Resources for assistance with field work. Thanks to Xianhua Li, Wenjun Li, and Bingyu Gao for help with the lab analyses. Thanks also to Galen P. Halverson and Changle Wang for geochemical guidance, Tor Grenne for help in recalculating detrital-free bulk compositions and John Aleinikoff for geochronology suggestions. A China Scholarship Council (CSC) grant supported Z.L. K.O.K. acknowledges a NSERC Discovery Grant and L.J.R. a Vanier Canada Graduate Scholarship.

Author Contributions

The research was planned by L.-C.Z. and C.-J.X. Main ideas were inspired by K.O.K., N.J.P., J.F.S., and L.J.R. Manuscript preparation was spearheaded by Z.-Q.L., K.O.K., N.J.P., J.F.S., and L.J.R. Field work, and analytical and data processing, were assisted by Z.-Q.L., M.-T.Z., and M.-T.Z.

Additional Information

Supplementary information accompanies this paper at <https://doi.org/10.1038/s41598-018-28187-2>.

Competing Interests: The authors declare no competing interests.

Publisher's note: Springer Nature remains neutral with regard to jurisdictional claims in published maps and institutional affiliations.



Open Access This article is licensed under a Creative Commons Attribution 4.0 International License, which permits use, sharing, adaptation, distribution and reproduction in any medium or format, as long as you give appropriate credit to the original author(s) and the source, provide a link to the Creative Commons license, and indicate if changes were made. The images or other third party material in this article are included in the article's Creative Commons license, unless indicated otherwise in a credit line to the material. If material is not included in the article's Creative Commons license and your intended use is not permitted by statutory regulation or exceeds the permitted use, you will need to obtain permission directly from the copyright holder. To view a copy of this license, visit <http://creativecommons.org/licenses/by/4.0/>.

© The Author(s) 2018